Research Square

Preprints are preliminary reports that have not undergone peer review.
They should not be considered conclusive, used to inform clinical practice,
or referenced by the media as validated information.

Quantitative comparison of CT-free attenuation correction frameworks of PET imaging in LAFOV PET/CT systems

Konstantinos D. Vrakidis

k.d.vrakidis@amsterdamumc.nl

Amsterdam UMC, Amsterdam, The Netherlands https://orcid.org/0009-0002-3527-9446

Maqsood M. Yaqub

Amsterdam UMC, Amsterdam, The Netherlands https://orcid.org/0000-0003-2122-740X

Mohammadreza Teimoorisichani

Siemens Medical Solutions USA, Inc.

Charlotte L.C. Smith

Amsterdam UMC, Amsterdam, The Netherlands

Marijke E. den Hollander

Amsterdam UMC, Amsterdam, The Netherlands

Catharina W. Menke-van der Houven van Oordt

Amsterdam UMC, Amsterdam, The Netherlands https://orcid.org/0000-0002-5404-5883

Idris Bahce

Amsterdam UMC, Amsterdam, The Netherlands https://orcid.org/0000-0002-1111-608X

Josee M. Zijlstra

Amsterdam UMC, Amsterdam, The Netherlands https://orcid.org/0000-0003-1074-5922

Gerben J.C. Zwezerijnen

Amsterdam UMC, Amsterdam, The Netherlands https://orcid.org/0000-0002-9571-9362

Ronald Boellaard

Amsterdam UMC, Amsterdam, The Netherlands https://orcid.org/0000-0002-0313-5686

Research Article

Keywords: LAFOV PET/CT, CT-Free, LSO-Tx, AI

Posted Date: October 2nd, 2026

DOI: https://doi.org/10.21203/rs.3.rs-8990485/v2

License: This work is licensed under a Creative Commons Attribution 4.0 International License.
Read Full License

Additional Declarations: The authors declare potential competing interests as follows: Mohammadreza Teimoorisichani is a full-time employee of Siemens Medical Solutions USA, Inc.. Ronald Boellaard has received a research grant from Siemens Healthineers.

Quantitative comparison of CT-free attenuation correction frameworks of PET imaging in long axial field-of-view PET/CT systems

Konstantinos D. Vrakidis[1,2*], Maqsood M. Yaqub[1,2], Mohammadreza Teimoorisichani[3], Charlotte L.C. Smith[1,2], Marijke E. den Hollander[1], Catharina W. Menke-van der Houven van Oordt[2,4], Idris Bahce[2,5,], Josée M. Zijlstra[2,6], Gerben J.C. Zwezerijnen[1,2], Ronald Boellaard[1,2]

[1]Department of Radiology and Nuclear Medicine, Vrije Universiteit Amsterdam, Amsterdam UMC, Amsterdam, The Netherlands

[2]Imaging and Biomarkers, Cancer Center Amsterdam, Amsterdam, The Netherlands

[3]Siemens Medical Solutions USA, Inc.

[4]Department of Medical Oncology, Vrije Universiteit Amsterdam, Amsterdam UMC, Amsterdam, The Netherlands

[5]Department of Pulmonary Medicine, Vrije Universiteit Amsterdam, Amsterdam UMC, Amsterdam, The Netherlands

[6]Department of Hematology, Vrije Universiteit Amsterdam, Amsterdam UMC, Amsterdam, The Netherlands

***Corresponding author**: Konstantinos D. Vrakidis (k.d.vrakidis@amsterdamumc.nl)

https://orcid.org/0009-0002-3527-9446

Disclaimer: Mohammadreza Teimoorisichani is a full-time employee of Siemens Medical Solutions USA, Inc.

Financial support: This work was financially supported by Siemens Healthineers.

Abstract

Objective: High sensitivity of long axial field-of-view (LAFOV) PET/CT systems enables diagnostic PET imaging with substantially reduced injected activity, increasing the relative contribution of CT to overall radiation exposure. Although multiple CT-free PET frameworks have been proposed, differences in evaluation methodology, including the use of scan-specific CT-information for precise patient-bed placement or for image registrations to handle PET-CT misalignments, complicate direct performance comparisons. This study performed a unified, CT-independent evaluation of CT-free frameworks for quantitative ^{18}F-FDG LAFOV PET imaging.

Methods: Six CT-free attenuation correction frameworks were investigated using the same non-curated patient dataset. Two attenuation-map (μ-map) generation approaches were first evaluated: a physics-based one in which transmission scans were performed using the intrinsic background radiation of lutetium oxyorthosilicate scintillators (LSO-Tx), eventually generating $\mu_{\text{LSO-Tx}}$, and a data-driven approach in which a convolutional neural network (CNN) synthesized μ_{CNN} from non-attenuation-corrected (NAC) PET image. Additional physics-based enhancements of both approaches were investigated by independently using the maximum likelihood-based reconstruction algorithms of activity and attenuation (MLAA) or attenuation correction factors (MLACF), generating the physics-based $\mu_{\text{LSO-Tx}}^{\text{MLAA}}$ and $\mu_{\text{LSO-Tx}}^{\text{MLACF}}$, and the data-physics hybrids of $\mu_{\text{CNN}}^{\text{MLAA}}$ and $\mu_{\text{CNN}}^{\text{MLACF}}$. Framework performances were evaluated using SUV_{mean} extracted from attenuation-corrected PET images.

Results: CNN-based frameworks demonstrated substantially lower SUV_{mean} biases than LSO-Tx-based approaches. Biases (mean ± standard deviation) for standalone, MLAA-, and MLACF-enhanced CNN frameworks were -9±7%, -12±13%, and -1.6±10.2%, respectively, compared with 29±29%, 26±100%, and 15±15% for the corresponding LSO-Tx frameworks. Low-attenuating objects located outside the patient body, including immobilization equipment and clothing, introduced median SUV_{mean} biases of approximately 6%. Localized attenuation-map inaccuracies generated by CNN or LSO-Tx, such as missing internal air-pockets or metal implants, were partially corrected by MLAA and MLACF.

Conclusion: Among the investigated CT-free frameworks, the hybrid framework that combined NAC-PET-based deep learning with MLACF enhancement achieved the highest quantitative accuracy. The unified CT-independent evaluation further demonstrated that low-attenuating objects substantially influence PET quantification and should be explicitly considered in future development and evaluation of CT-free PET frameworks.

Keywords: LAFOV PET/CT, CT-Free, LSO-Tx, AI

Introduction

Quantitative positron emission tomography (PET) conventionally relies on X-ray computed tomography (CT), or its low-dose variant (LD-CT), for attenuation and scatter correction. Although the radiation burden from LD-CT is generally modest compared to that of a typical [^{18}F]-fluorodeoxyglucose (^{18}F-FDG) PET/CT examination (*1*), CT remains an additional source of ionizing radiation and a persistent contributor to visual or quantification errors in PET through mismatches due to motion, metal artifacts, and photon starvation effects associated with aggressive dose-reduction strategies such as tin filtration (*2*,*3*). These limitations are becoming increasingly relevant with the emergence of long-axial field-of-view (LAFOV) PET/CT systems, whose substantially increased sensitivity enables diagnostic-quality PET imaging at only a fraction of the standard injected activities (*4*). As PET moves towards ultra-low-dose imaging, particularly in children, pregnant patients, and healthy volunteers, the relative contributions of CT to the overall radiation exposure and to quantitative inaccuracies become increasingly significant. Consequently, CT-free PET imaging frameworks are attracting interest as an alternative pathway to quantitative PET imaging, not only for standalone PET or hybrid magnetic resonance (PET/MR) systems, but potentially also as an enabling technology for ultra-low-dose PET applications.

Existing CT-free frameworks can broadly be categorized into physics-based reconstruction approaches and data-driven artificial intelligence (AI)-based ones. For physics-based approaches, maximum likelihood-based reconstruction algorithms that simultaneously estimate of the activity and attenuation (MLAA) (*5*,*6*) or activity and attenuation correction factors (MLACF) (*7–9*) have been pivotal. Combined with anatomical priors obtained by performing a transmission scan based on the intrinsic radioactivity of the lutetium oxyorthosilicate scintillator crystals (LSO-Tx), promising performance has been demonstrated (*10*,*11*). In parallel, several AI-based CT-free frameworks have been investigated in LAFOV PET that typically rely on data to train deep convolutional neural networks (CNN) to synthesize either linear attenuation coefficient maps (μ-maps) (*12*,*13*) or directly corrected PET images (*14*,*15*) by using different inputs, such as non-attenuation corrected (NAC) PET images (*13–15*), or even MLACF-enhanced LSO-Tx (*12*). While AI-based methods show promise in standardized uptake value (SUV) quantification, they require tracer-specific training and their generalizability remains a challenge (*16*).

Key methodological differences across the plethora of the proposed CT-free PET imaging techniques challenge direct comparisons in quantitative performance. For instance, the impact of low-attenuating objects (LAOs) located outside of patient, such as immobilization equipment or even hair, is often not explicitly addressed (*12*,*14*,*15*,*17*,*18*), despite being unique to each patient scan and potentially introducing quantification biases of over 10% (*19–21*). Occasionally, information from the CT is used during evaluations for inserting the patient bed or LAOs (*13*,*22*), and for image registrations to handle PET-CT misalignments (*12*). In addition, evaluations on independent datasets might also introduce population-based biases and potentially mask performance characteristics or irregularities under a biological component. Consequently, comparative evidence on the relative advantages and limitations of major CT-free PET framework categories, such as physics-based or data-driven, remains limited.

In this work, we performed a head-to-head comparison of six fundamentally distinct CT-free frameworks for clinical ^{18}F-FDG PET imaging on a LAFOV PET/CT system. The primary objective was to compare the quantitative performance of these frameworks relative to the CT-based framework. The secondary objective was to characterize framework-specific advantages, limitations, and failure modes. All methods were evaluated using a unified, CT-independent workflow on the same non-curated patient dataset to assess performance under clinically realistic

conditions. The frameworks combined LSO-Tx- or AI-based μ-map estimation with or without MLAA or MLACF enhancement, representing physics-based, data-driven, and hybrid approaches.

Methods

Data

Retrospective ^{18}F-FDG PET/CT data from two patient cohorts were used for this study, with their demographics provided in the Supplementary Table 1. All emission and transmission data were acquired at Amsterdam UMC, location VUmc, with the Biograph Vision Quadra LAFOV PET/CT scanner (Siemens Healthineers, Knoxville TN, USA), which has 106 cm axial FOV and 220 ps TOF resolution, using three distinct imaging protocols (Figure 1).

The first cohort, consisted of 114 oncological patients who underwent protocol A in the context of standard clinical care, was used for the development of the AI-based frameworks. The cohort (58 men, 56 women, with mean±standard deviation of 63±13 years age and of 74.7±13.8 kg weight) was injected with 3.1±0.7 MBq/kg of ^{18}F-FDG and scanned one hour post injection (p.i.). Protocol A was consisted of a LD-CT, followed by a static single-bed whole body PET acquisition of 8 minutes. The institutional review board approved this retrospective study (approval number 2018.029) and the requirement to obtain informed consent was waived. The cohort was split into training and validation datasets of 100 and 14, respectively.

The second cohort, reserved for testing the investigated CT-free frameworks, was consisted of 12 patients with various diseases that additionally underwent an LSO-Tx scan. These patients (4 men, 8 women, aged 59±11 and weighted 72±18 kg) were injected with 3.1±0.3 MBq/kg of ^{18}F-FDG and then scanned either by an 8-minute static PET protocol acquired one hour p.i. or by a 70-minute dynamic PET protocol (protocols B and C in Figure 1, respectively), both followed by a 5-minute LSO-Tx scan. The study was approved by the institutional review board (approval numbers NL80924.029.22, 2022.0230), and a written informed consent was signed from all patients. For Protocol C, the 57-65 min p.i.. interval was selected to match the average start time (57 min p.i.) and 8-min duration of the clinical acquisitions used for CNN development. To record the coincidence events for the LSO-Tx scan, the methodology described in the work of Teimoorisichani et al. was used (*11*). While acquiring LSO-Tx data during the PET scan is technically feasible (*11*), we were required to perform them separately and after concluding the clinical examination to ensure no interference with the clinical workflow.

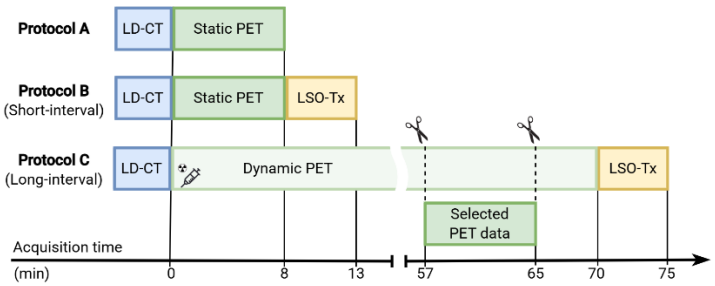


Figure 1. The three whole-body ^{18}F-FDG PET/CT imaging protocols used. CT-free frameworks were assessed based on scans acquired with protocols B and C, which are respectively characterized by the short and the long time-intervals between LD-CT and the PET acquisitions.

Outline of frameworks

In this study, six CT-free μ-map generating PET frameworks were compared with the CT-based PET framework, which served as the current clinical reference (Figure 2). For the reference framework, CT-based μ-maps (μ_{CT}) were reconstructed from the acquired LD-CT data using the maximum-likelihood transmission reconstruction (MLTR) algorithm (*23*). For the first CT-free framework, LSO-Tx data were histogrammed in non-TOF sinograms (*10*,*11*) that were subsequently reconstructed to μ-maps ($\mu_{LSO\text{-}Tx}$) with MLTR (*23*), according to the methodology of Teimoorisichani et al. (*11*).

For the second framework, a five-level 3D attention-gated U-Net implemented in MONAI (24,25) synthesized μ-maps (μ_{CNN}) from NAC-PET. NAC-PET and μ_{CT} were resampled to 3.3-mm voxels, normalized, and contrast- and edge-enhanced. Training used 128^3-voxel patches, L1 loss, AdamW optimization, an initial learning rate of 10^{-4}, and no data augmentation. The complete architecture and training details are provided in the Supplementary Methods.

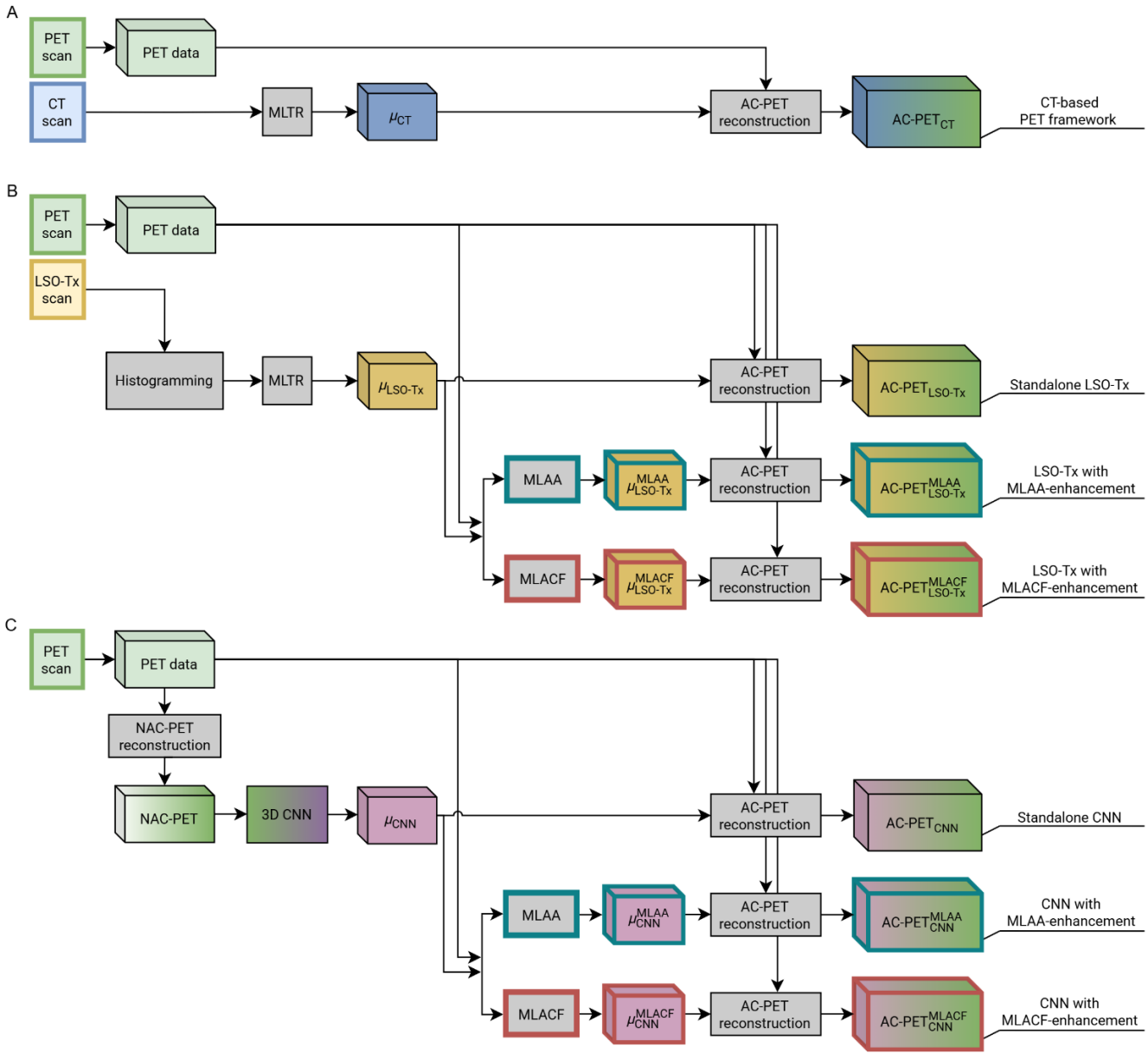


Figure 2. Flowcharts of the CT-based (A) and the six CT-free PET imaging frameworks investigated, which were grouped in (B) LSO-Tx based and (C) CNN-based frameworks.

The remaining four frameworks investigated the potential enhancement using the TOF-enabled MLAA and MLACF joint-reconstruction algorithms. MLAA and MLACF were applied independently to the emission data using either $\mu_{\text{LSO-Tx}}$ or μ_{CNN} as priors, yielding $\mu_{\text{LSO-Tx}}^{\text{MLAA}}$, $\mu_{\text{LSO-Tx}}^{\text{MLACF}}$, $\mu_{\text{CNN}}^{\text{MLAA}}$, and $\mu_{\text{CNN}}^{\text{MLACF}}$ (*11*,*12*). MLAA and MLACF were used with fixed reconstruction settings across all patients and μ-map priors, using 20 and 30 global iterations, respectively. Activity images estimated by MLAA and MLACF were not used because their intensity scales differed from CT-based AC-PET images (*11*). The complete reconstruction and regularization parameters are provided in the Supplementary Methods.

In all CT-free μ-maps, the generated patient bed μ-values were replaced through template matching with a bed template segmented form a blank LD-CT acquisition, ensuring that no patient-specific CT information was introduced into the CT-free workflows.

Attenuation and scatter corrections were independently calculated from each μ-map and were applied during the reconstruction of emission data, yielding corrected PET images (AC-PET). These reconstructions used the ordinary Poisson ordered subsets expectation-maximization algorithm (e7-tools, Siemens Healthineers), with 4 iterations, 5 subsets, maximum ring difference of 85, point-spread-function modeling, and relative-scaled 3D TOF single-scatter simulation (*26*).

Analysis

CT-free frameworks were evaluated against the CT-based reference using Protocols B and C, neither of which was used for CNN training. μ-maps and AC-PET images were visually inspected for metal, motion, emission-transmission cross-talk, and AI-related inaccuracies. Because Protocols B and C differed in time-intervals between LD-CT and PET, alignment was additionally quantified using the Dice similarity coefficient (DSC) between PET- and CT-derived body contours, with higher DSC indicating greater spatial overlap. A blinded PET/CT-trained reader also attempted to identify AC-PET_{CT} among two CT-free reconstructions and assessed lesion detectability.

Mean μ-values and SUV (SUV_{mean}) were extracted using volumes of interest (VOIs). Ten spherical healthy-tissue VOIs (20-30 mm) and up to three lesion VOIs per patient were delineated on AC-PET_{CT} and transferred to all reconstructions. Since only 5 patients had more than three lesions, lesion VOIs were limited to three to maintain data balance. Lesion VOIs were generated using a semi-automatic region-growing method, initiated at the voxel of maximum uptake, with neighboring voxels included if within 60% of this value. Details and visualizations of the lesion VOIs can be found in the Supplementary Data (Table 2, Figure 1). No VOIs were placed proximal to metal implants to avoid biases from CT-based streak artifacts. Liver coefficients of variation (CV) and lesion contrast-to-noise ratios (CNR) (*27*) were also calculated.

Paired differences and relative differences from the CT-based reference were reported in SUVs or percentages and summarized as mean±SD or median (Q1,Q3), depending on distribution normality. For statistical testing, two-sided Wilcoxon signed-rank tests with Bonferroni correction were used. Frameworks were additionally compared using root sum of squares (RSS):

$$RSS = \sqrt{(mean(\Delta))^2 + (SD(\Delta))^2}$$

where Δ denotes the paired CT-free-CT difference of μ-values, SUV_{mean} , CV or CNR. RSS provides a descriptive composite of bias magnitude and dispersion, with lower values indicating closer and more consistent agreement with the CT-based reference. Bland-Altman analysis was performed for the framework with the lowest overall RSS.

Investigations of low-attenuating objects

Objects placed outside the patient body are not reliably generated in μ-maps of the investigated CT-free frameworks due to a lack of tracer uptake. To investigate their impact on PET quantification, the quantitative analyses of CT-free frameworks were repeated with CT-based μ-values of these objects manually inserted into the μ-maps (Supplementary Data). Since patient scan-specific CT-based information was used, these frameworks, annotated with "†", do not represent fully CT-free ones.

Results

Qualitative analysis

Test cases of μ-maps generated by both CT-based and CT-free methods and their corresponding PET images can be seen in Figure 3. Visually in $\mu_{\text{LSO-Tx}}$, the body contours of patients were approximated but without managing to generate discernable anatomical structures and with an overall μ-value overestimation. Both MLAA and MLACF restored discernable anatomical structures such as bones, lung tissue or air cavities in the abdomen. The metal hip implants (Figure 3), which caused streak artifacts in μ_{CT} and were not visible in $\mu_{\text{LSO-Tx}}$, were partially recovered after using MLAA and MLACF. Cross-talk artifacts were observed in $\mu_{\text{LSO-Tx}}^{\text{MLAA}}$ and $\mu_{\text{LSO-Tx}}^{\text{MLACF}}$ of all patients at regions with high ^{18}F-FDG uptake, such as the brain gray matter or the urinary bladder. Visually, the standalone CNN μ-maps were smoother than μ_{CT} and showed reduced bone-to-soft-tissue contrast, while adipose tissue and muscle remained distinguishable. Compared with μ_{CT}, all metal implants and, occasionaly, internal air cavities, were absent or only partially reproduced. The enhancements of μ_{CNN} with MLAA or MLACF introduced noise and cross-talk artifacts in all patient cases, however they were also found to partially recover in multiple patient cases metal implants and air cavities. In all CT-free μ-maps, low-attenuating objects, such as head pillows or clothing, were not reliably generated.

In AC-PET images (Figure 3), large overestimations were observed in regions of high ^{18}F-FDG uptake in case of AC-PET$_{\text{LSO-Tx}}$ and AC-PET$_{\text{LSO-Tx}}^{\text{MLACF}}$, while understimations of the same magnitude were observed in case of AC-PET$_{\text{LSO-Tx}}^{\text{MLAA}}$ and AC-PET$_{\text{CNN}}^{\text{MLAA}}$. Only minor differences from the AC-PET$_{\text{CT}}$ were found in AC-PET$_{\text{CNN}}$ and AC-PET$_{\text{CNN}}^{\text{MLACF}}$. In the blinded qualitative evaluation (Supplementary Table 3), the trained reader could correctly identify AC-PET$_{\text{CT}}$ among AC-PET$_{\text{CNN}}$ and AC-PET$_{\text{CNN}}^{\text{MLACF}}$ images of the same patient with only 17% (2/12) accuracy, with the rest of the cases being incorrectly classified or visually indistinguishable. In the same evaluation, organ visibility and lesion detectability were found the same across AC-PET images, with the exception of the occasional presence of artifacts around the bladder or the lack of breathing artifacts at the liver dome in AC-PET$_{\text{CNN}}^{\text{MLACF}}$ (Supplementary Figure 2).

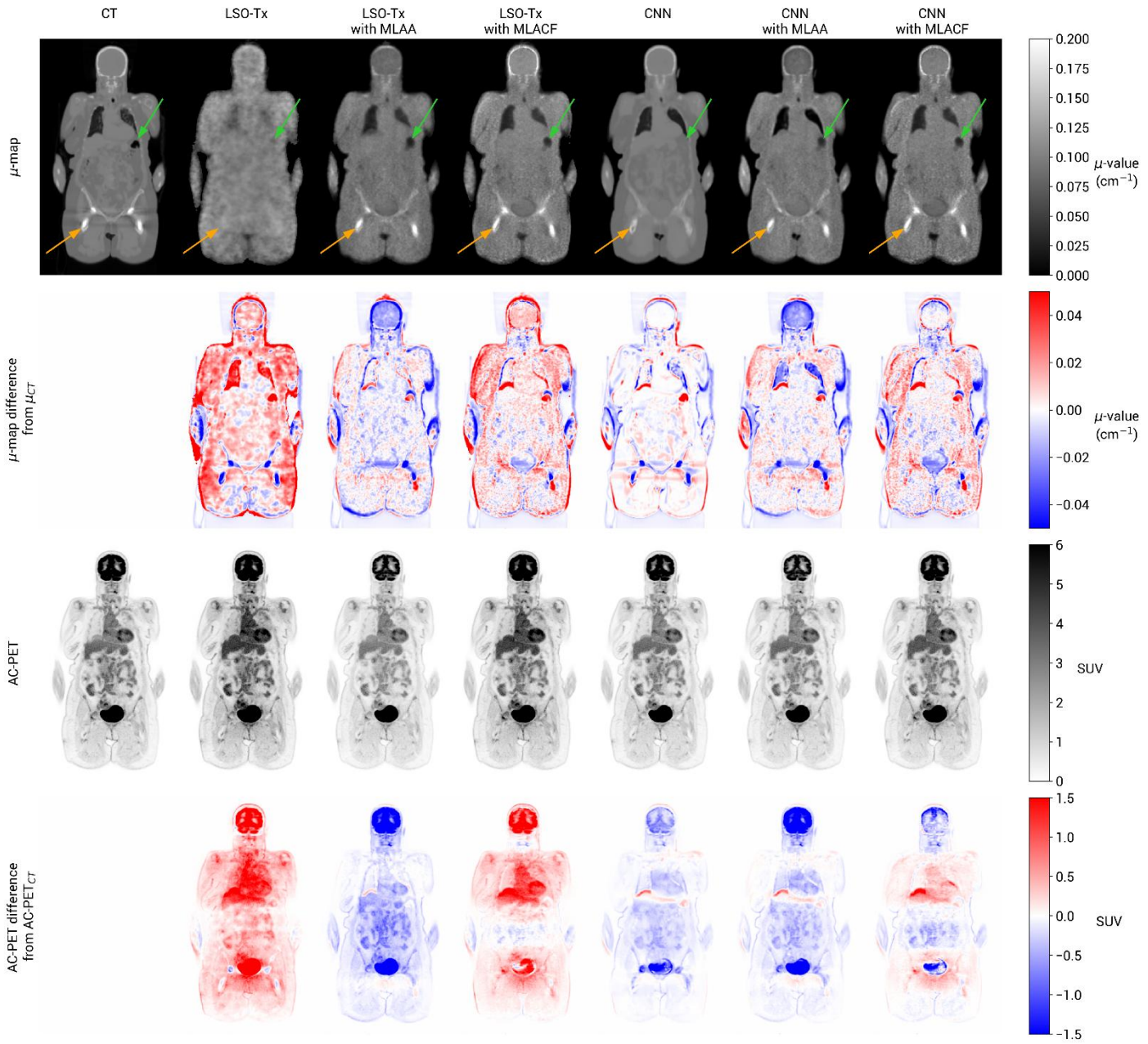


Figure 3. Coronal slices of μ-maps and their equivalent *AC-PET* images as produced by the CT-based and the six CT-free frameworks of a patient (76 kg, 31 body mass index) acquired using protocol C with long time-interval between LD-CT and PET. μ-values of metal implants and air cavities, which are respectively annotated with orange and green arrows on μ-maps, differ in each framework.

Quantitative analysis

The results of the VOI-based analyses can be found in Supplementary Data (Table 4 for μ-maps, Tables 5, 6, and Figure 3 for AC-PET images), with an overview of the AC-PET analysis depicted in Figure 4. Overall in healthy organs, significant SUV_{mean} differences from $AC\text{-}PET_{CT}$ were obtained from LSO-Tx with 21% (12%,45%), from LSO-Tx with MLACF with 14% (7%,24%), from CNN with -8.1% (-11%,-5.2%), and from CNN with MLAA -10% (-20%,-2.1%). The biases of -2% (-14%,8.6%) and 1.6% (-5.7%,3.4%) of the LSO-Tx with MLAA and the CNN with MLACF frameworks were not significant, with *P*-values of 0.74 and 0.19, respectively. Combining bias and variance with RSS, comparably low values were measured with the standalone-CNN and the CNN with MLACF frameworks. Additional comparisons performed (Supplementary Table 7) show that MLACF provided significantly improved quantification in the ascending aorta, white matter, liver, lung, spleen, and lesions, while also significantly worse quantification in the adipose and muscle tissues.

In lesion quantification, significant differences were measured with LSO-Tx at 21% (8%,30%), with standalone-CNN at -10% (-17%,-7%), with CNN-MLAA at -14% (-20%,-11%), and with CNN-MLACF at -8.7% (-13%,-2.1%). Contrary, the biases of -6% (-13%,8.6%) from LSO-Tx with MLAA and of 3.5% (-4.1%,14%) from LSO-Tx with MLACF were found non-significant, with *P*-values of 0.61 and 0.069, respectively. The CNN with MLACF framework had the lowest RSS.

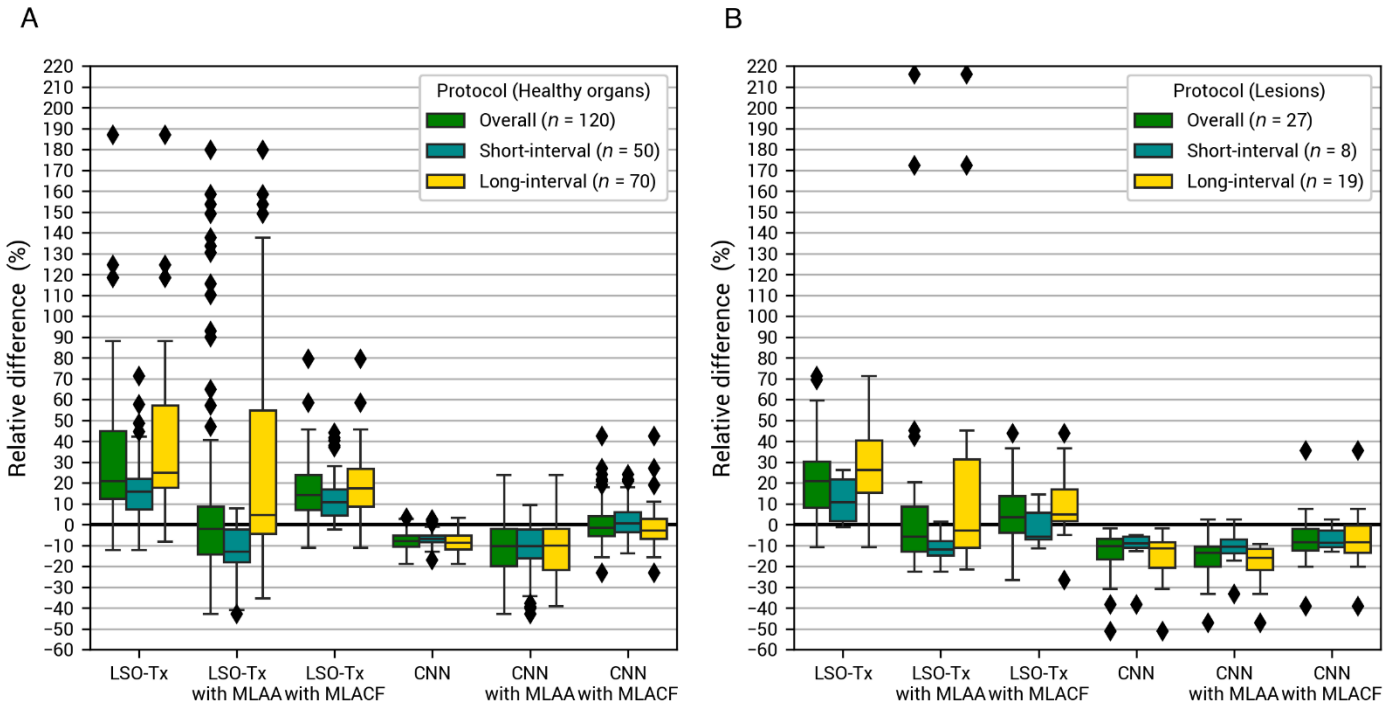


Figure 4. Box-plots with whiskers of relative differences in SUV_{mean} between CT-free and the reference CT-based PET frameworks, **(A)** for healthy organs and **(B)** for lesions.

Short vs long time-intervals

Quantification errors were larger in the long-interval cohort, reflected by higher RSS values driven by increased biases, variances, or both, especially in LSO-Tx-based frameworks. The CNN-MLACF framework, which had the highest SUV_{mean} agreements to the CT-references in both types of data, yielded median (range, RSS, *P*-value) differences of -1.5% (-4.3%,4.7%, 8.5, 0.86) for short-interval data and -3.3% (-8.3%,1.6%, 11.3, <0.001) for long-interval data, across all VOIs. Visual inspection found that 70% (5/7) of the long time-interval scans exhibited misalignments between AC-PET_{CT} and μ_{CT}, especially at the arms (Supplementary Figure 4), while none such mismatches were found in the short time-interval ones. Consistently, mean PET-CT body-contour DSC was lower in the long-interval Protocol C than in the short-interval Protocol B (0.956±0.015 vs 0.978±0.008, *P*-value=0.003), quantitatively confirming greater global PET-CT mismatch. Body mass indices were also higher in the long-interval cohort (26.1±4.3 vs. 23.6±2.9).

Image noise and lesion CNR

Significant increases in CVs over the CT-reference were measured in all CT-free μ-maps except of the μ_{CNN} that had a significant 30% decrease (Figure 5, Supplementary Table 8). In AC-PET images, no significant differences in CVs were measured. A significant decrease in lesion CNR was measured for all CT-free frameworks, with the exception of the standalone-CNN one (*P*=0.086). The magnitudes of the CNR decreases were (mean±sd) 1.9±2.1% in LSO-Tx, 5±8% in LSO-Tx with MLAA, 5±8% in LSO-Tx with MLACF, 6±8% in CNN with MLAA, and 5±8% in CNN with MLACF.

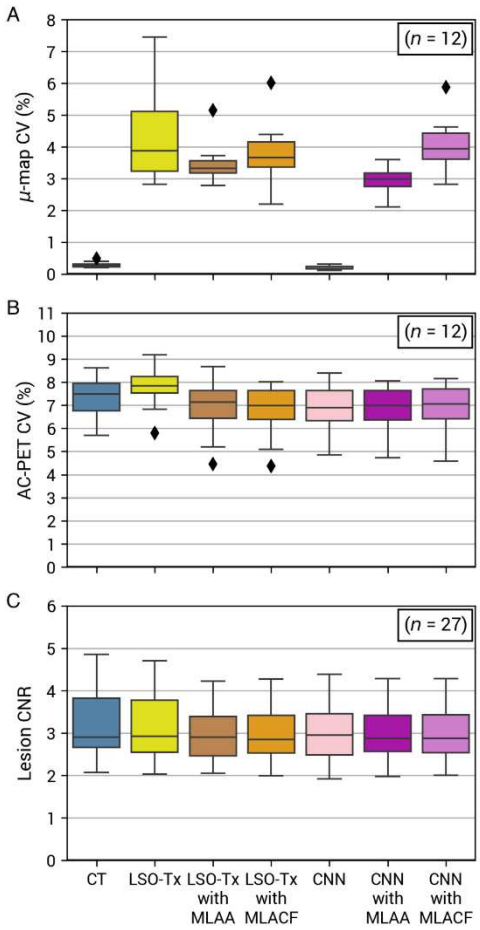


Figure 5. Box-plots with whiskers of coefficients-of variation in μ-maps (A) and AC-PET images (B), as well as of lesion contrast-to-noise ratio (C).

Organ-based analysis

Focusing on the CNN with MLACF framework that exhibited the lowest overall RSS, we assessed performance across VOIs using Bland-Altman analysis (Supplementary Figure 5), after confirming first the normality of differences with QQ-plots. Biases of under 0.2 SUV with limits of agreement within ±0.4 SUV were measured in all organs with the exception of liver, gray matter, and lesions. In liver, slightly wider limits were found (±0.6 SUVs). The largest deviations occurred in grey matter and lesions, with mean biases at -1.0 and -0.6 SUVs, and limits at ±1.2 and ±2.0, respectively. Inspection of the largest lesion SUV outliers identified potential contributions from PET-CT misalignment, small VOI size, and a metallic cardiac pacemaker (Supplementary Figure 6).

Impact of low-attenuating objects

Items identified as LAOs included head and leg pillows, clothing, immobilization straps, and a post-mastectomy prosthesis. Based on μ_{CT}, these were estimated to have an average μ-value of (6.2±6.7)×10^{-3} cm^{-1} over a volume of 22.4±6.9 liters, excluding the patient bed. By inserting CT-based μ-values of LAOs, significant improvements in SUV_{mean} quantification were obtained, especially in grey matter and lesions (Figure 6). Respectively, biases were reduced to -0.8% (-1.7%,0.3%) and -3.8% (-10.7%,-1%) using the CNN† framework, and to 0.4% (-4.2%,2.9%) and -0.6% (-8.1%,3.7%) using the CNN-MLACF† one. Across all frameworks, unaccounted LAOs led to SUV_{mean} underestimations of 5.9% (3.5%,8.3%) (Supplementary Tables 9 and 10).

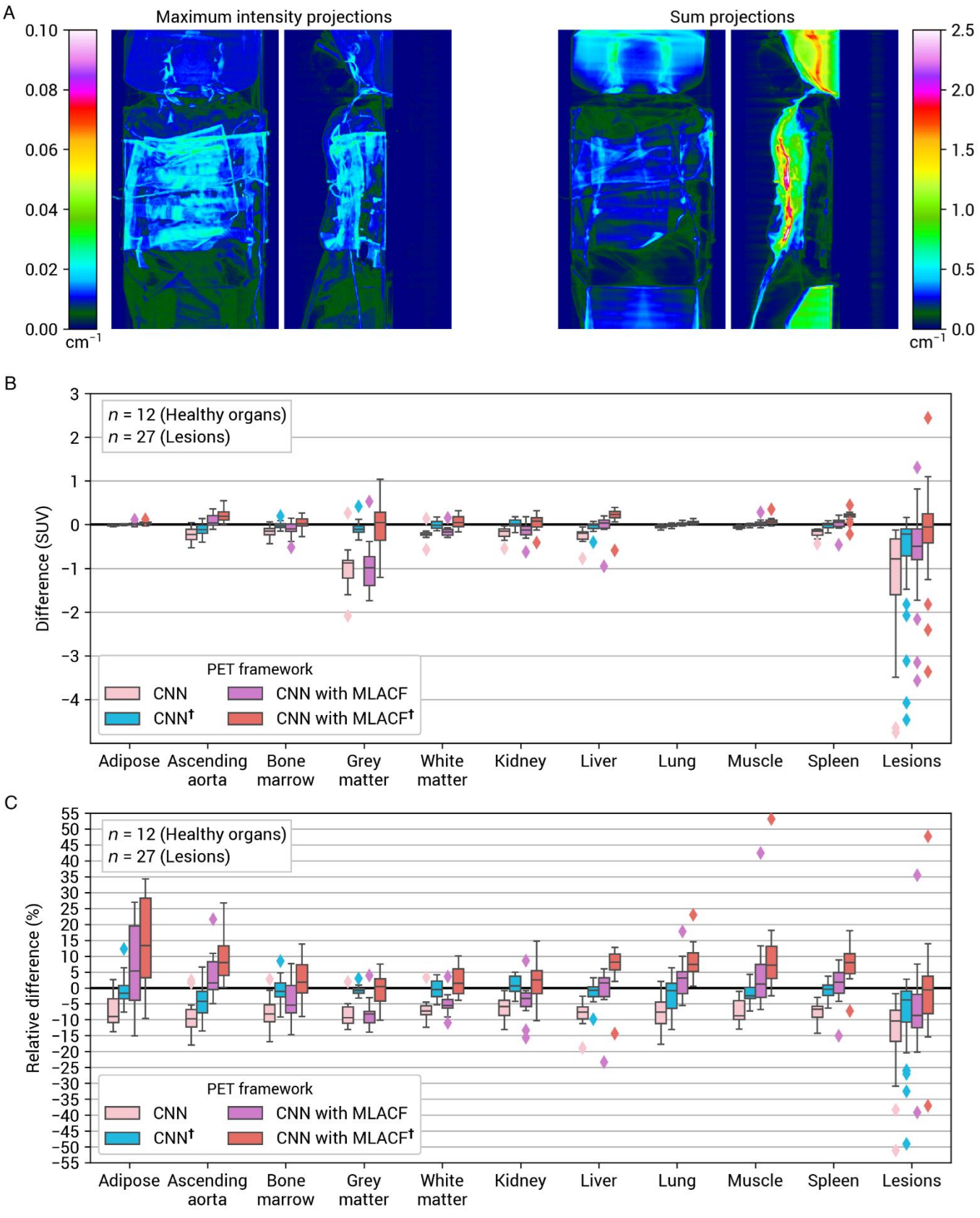


Figure 6. (A) Maximum intensity projections and sum projections of μ_{CT} after masking out the patient body and isolating the LAOs. Objects such as immobilization straps, clothing, head and leg pillows can be observed. Box-plots with whiskers of differences (B) and relative differences (C) in SUV_{mean} between the reference CT-based PET framework and the CNN, MLACF with CNN, and their CT-dependent counterparts (†) with substituted LAO μ-values from the μ_{CT}.

Discussion

Among the six CT-free PET frameworks evaluated, the CNN with MLACF demonstrated the best overall SUV_{mean} agreement to the CT-based reference, with a median difference (interquartile range) of -0.03 (-0.14, 0.04) SUVs or -2.6% (-7.3%, 3.4%), across all VOIs.

The largest SUV_{mean} deviations across all frameworks were observed in grey matter and lesions. For the MLACF-enhanced CNN framework, mean biases respectively reached approximately -1 SUV (-8%) and -0.6 SUV (-7%). A major contributor to these inaccuracies was the inability of all frameworks to reliably generate μ-values of LAOs, such as positioning equipment and clothing, whose presence and configuration varied across patient examinations. Despite their low μ-values (~0.01 cm^{-1}), their large spatial extent made them non-negligible contributors to photon attenuation and scatter, resulting in median SUV_{mean} underestimations of 5.9% (3.5%, 8.3%) across frameworks when left unaccounted. Similar quantification effects caused by missing positioning aids, headphones or flexible radiofrequency coils have previously been reported in brain PET/MR studies (*19–21*). However, most recent CT-free PET investigations do not explicitly report the presence or handling of such objects. These findings suggest that LAOs represent an important but frequently overlooked source of quantification bias. These limitations of current CT-free PET frameworks can be overcome by e.g. using attenuation templates with standardized immobilization devices.

To compare with previous literature, LAOs were inserted into μ-maps, improving lesion quantification for CNN-MLACF† and CNN† to mean SUV_{mean} biases of -1.5±13.7% and -9.1±12.6%, respectively. The lesion-level performance of CNN† remained lower than that reported by several NAC-PET-based AI frameworks (*17*,*18*,*22*). This difference may partly reflect the longer PET-CT interval in the dynamic scans, which increased misregistration and may have introduced bias through the CT-based reference. Restricting the analysis to short-interval static scans reduced the CNN† lesion bias to -5.2±10.6%. In the same cohort, healthy-organ and grey-matter biases were -0.6±5.1% and -1.4±1.0%, respectively, comparable to state-of-the-art approaches (*13*,*15*,*17*,*18*,*22*).

An advantage of MLACF enhancement compared to using standalone CNN is a possible improved estimation of μ-values of metal implants, internal air pockets, and bones structures. These issues are known challenges for NAC-PET CNN or AI attenuation methods due to limited ^{18}F-FDG uptake and their limited or spatially variable presence in the training data (*11*,*13*,*22*). MLACF was also observed to elevate tissue μ-values in regions close to missing LAOs (Supplementary Figure 7), suggesting a possible compensatory characteristic. These observations suggest that physics-based reconstruction approaches can mitigate localized μ-map inaccuracies arising from AI based attenuation correction approaches.

Direct comparisons between the LSO-Tx-based frameworks and their CNN-based counterparts demonstrated significantly improved overall SUV_{mean} quantification using the standalone and MLACF-enhanced CNN approaches. MLAA-enhanced LSO-Tx and CNN yielded comparable performance, although the former occasionally produced severe hyperintense μ-map artifacts that propagated into the attenuation-corrected PET images (Supplementary Figure 4). Nevertheless, LSO-Tx frameworks, particularly when combined with joint-reconstruction algorithms (*11*) or with AI (*12*), remain promising because of their physics-based nature, which may provide greater robustness in scenarios that are underrepresented in CNN training data, such as in atypical patient anatomies.

One advantage of emission-only approaches is their spatial alignment with the average tracer distribution and patient position during PET acquisition, avoiding PET-CT misregistration errors. In the long-interval cohort, 70% of scans

showed visible PET-CT mismatch and had significantly lower body-contour DSC compared to short-interval scans, whereas CT-free μ-map body contours remained aligned with the PET data (Supplementary Figure 4). SUV_{mean} biases were consistently larger in the long-interval cohort across all frameworks. Since the misregistration-sensitive CT-based framework was used as reference, misalignment-driven biases may have penalized CT-free methods despite providing μ-maps with better alignment with PET images. Additionally, the elevated bladder activity in long-interval examinations, can affect the LSO-Tx performance (*11*), challenge CNNs by distorting NAC-PET contrast, and intensify MLAA/MLACF cross-talk artifacts (*11*,*12*). These findings support that dynamic PET protocols with long-time interval between PET and CT are useful tests of PET attenuation-correcting frameworks under motion and physiologic variability.

This work has several limitations. CT-based attenuation correction was used as the reference rather than an absolute ground truth, as it remains susceptible to PET-CT misregistration and CT-related artifacts. Consequently, some observed differences may actually reflect improvements of the CT-free frameworks compared with the CT based one. The frameworks were tested on a relatively small dataset of 12 FDG PET/CT studies. However, we applied all frameworks to all patients allowing for a direct head-to-head comparison, including the LSO background method. Yet, validation on larger cohorts, scans with lower statistics and non-FDG tracers has not yet been widely performed and should be explored in future studies.

Conclusions

A hybrid CT-free PET framework combining AI-based attenuation estimation with MLACF enhancement achieved the highest quantitative agreement with CT-based reference data. Physics-based enhancements partially corrected gross attenuation-map errors, such as missing internal air pockets or metal implants. Substantial quantification biases can be introduced by low-attenuating objects, such as immobilization equipment and clothing, highlighting an often-overlooked limitation of CT-free PET approaches that necessitates accurate handling.

Abbreviations

AC: Attenuation-corrected
AI: Artificial intelligence
CNN: Convolutional neural network
CNR: Contrast-to-noise ratio
CT: Computed tomography
CV: Coefficient of variation
DSC: Dice similarity coefficient
FDG: Fluorodeoxyglucose
LAFOV: Long axial field of view PET
LAO: Low-attenuating object
LD-CT: Low dose CT
LOR: Line of response
LSO: Lutetium oxyorthosilicate
LSO-Tx: LSO-based transmission scan
MLAA: Maximum-likelihood activity and attenuation
MLACF: Maximum-likelihood activity and attenuation correction factors
MLTR: Maximum-likelihood transmission reconstruction
MR: Magnetic resonance
NAC: Non attenuation-corrected
p.i.: post-injection
PET: Positron emission tomography
Q1: The first quantile or 25th percentile
Q3: The third quantile or 75th percentile
RSS: Root sum of squares
SD: Standard deviation
SUV: Standardized uptake value
TOF: Time of flight
VOI: Volume of interest
***μ*-map:** Linear attenuation coefficient map

Statements & Declarations

Acknowledgements

We thank Veerle Kersemans, Deepak Bharkhada, Inki Hong, and Maurizio Conti (Siemens Healthineers) for insightful discussions.

Ethics approval

The data used in this work were obtained by studies that were approved by the institutional review board (IRB 2018.029 and NL80924.029.22, IRB 2022.0230), and written informed consents were obtained from the patients. The study was performed in accordance with the Declaration of Helsinki.

Consent for publication

Not applicable.

Availability of data and materials

Data are available upon reasonable request.

Competing interests

Mohammadreza Teimoorisichani is a full-time employee of Siemens Medical Solutions USA, Inc..
Ronald Boellaard has received a research grant from Siemens Healthineers.
There are no other conflicts of interest to report.

Funding

This research was financially supported by Siemens Healthineers.

Author contributions

Conceptualization: KV, MY, RB; data curation: KV, MY, CS, MdH, RB; formal analysis: KV; funding acquisition: RB; investigation: KV, MY, RB; methodology: KV, MY, MT, RB; project administration: CWM, IB, JZ, RB; resources: MY, MT, CS, MdH, CWM, IB, JZ, RB; software: KV, MT, RB; supervision: MY, RB; validation: KV, MY, RB; visualization: KV; writing-original draft: KV; writing-review and editing: KV, MY, CS, RB. All authors read and approved of the final manuscript.

References

1. Ferrara D, Shiyam Sundar LK, Chalampalakis Z, et al. Low-dose and standard-dose whole-body [18F]FDG-PET/CT imaging: implications for healthy controls and lung cancer patients. *Front Phys*. 2024;12.
2. Tsai Y-J, Liu C. Pitfalls on PET/CT due to artifacts and instrumentation. *Semin Nucl Med*. 2021;51:646-656.
3. Mostafapour S, Greuter M, van Snick JH, et al. Ultra-low dose CT scanning for PET/CT. *Med Phys*. 2024;51:139-155.
4. Calderón E, Schmidt FP, Lan W, et al. Image Quality and Quantitative PET Parameters of Low-Dose [18F]FDG PET in a Long Axial Field-of-View PET/CT Scanner. *Diagnostics*. 2023;13:3240.
5. Rezaei A, Defrise M, Bal G, et al. Simultaneous Reconstruction of Activity and Attenuation in Time-of-Flight PET. *IEEE Trans Med Imaging*. 2012;31:2224-2233.
6. Li Y, Matej S, Karp JS. Practical joint reconstruction of activity and attenuation with autonomous scaling for time-of-flight PET. *Phys Med Biol*. 2020;65:235037.
7. Panin VY, Aykac M, Casey ME. Simultaneous reconstruction of emission activity and attenuation coefficient distribution from TOF data, acquired with external transmission source. *Phys Med Biol*. 2013;58:3649.
8. Rezaei A, Defrise M, Nuyts J. ML-Reconstruction for TOF-PET With Simultaneous Estimation of the Attenuation Factors. *IEEE Trans Med Imaging*. 2014;33:1563-1572.
9. Salvo K, Defrise M. sMLACF: a generalized expectation-maximization algorithm for TOF-PET to reconstruct the activity and attenuation simultaneously. *Phys Med Biol*. 2017;62:8283.
10. Rothfuss H, Panin V, Moor A, et al. LSO background radiation as a transmission source using time of flight. *Phys Med Biol*. 2014;59:5483.
11. Teimoorisichani M, Panin V, Rothfuss H, Sari H, Rominger A, Conti M. A CT-less approach to quantitative PET imaging using the LSO intrinsic radiation for long-axial FOV PET scanners. *Med Phys*. 2022;49:309-323.
12. Sari H, Teimoorisichani M, Mingels C, et al. Quantitative evaluation of a deep learning-based framework to generate whole-body attenuation maps using LSO background radiation in long axial FOV PET scanners. *Eur J Nucl Med Mol Imaging*. 2022;49:4490-4502.
13. Montgomery ME, Andersen FL, d'Este SH, et al. Attenuation Correction of Long Axial Field-of-View Positron Emission Tomography Using Synthetic Computed Tomography Derived from the Emission Data: Application to Low-Count Studies and Multiple Tracers. *Diagnostics*. 2023;13:3661.
14. Li W, Huang Z, Chen Z, et al. Learning CT-free attenuation-corrected total-body PET images through deep learning. *Eur Radiol*. 2024;34:5578-5587.
15. Sun H, Huang Y, Hu D, et al. Artificial intelligence-based joint attenuation and scatter correction strategies for multi-tracer total-body PET. *EJNMMI Phys*. 2024;11:66.
16. Jha AK, Bradshaw TJ, Buvat I, et al. Nuclear medicine and artificial intelligence: best practices for evaluation (the RELAINCE guidelines). *J Nucl Med*. 2022;63:1288-1299.
17. Dong X, Wang T, Lei Y, et al. Synthetic CT generation from non-attenuation corrected PET images for whole-body PET imaging. *Phys Med Biol*. 2019;64:215016.
18. Shi L, Zhang J, Toyonaga T, Shao D, Onofrey JA, Lu Y. Deep learning-based attenuation map generation with simultaneously reconstructed PET activity and attenuation and low-dose application. *Phys Med Biol*. 2023;68:35014.
19. Mantlik F, Hofmann M, Werner MK, et al. The effect of patient positioning aids on PET quantification in PET/MR imaging. *Eur J Nucl Med Mol Imaging*. 2011;38:920-929.

20. Paulus DH, Tellmann L, Quick HH. Towards improved hardware component attenuation correction in PET/MR hybrid imaging. *Phys Med Biol*. 2013;58:8021.

21. Mackewn JE, Stirling J, Jeljeli S, et al. Practical issues and limitations of brain attenuation correction on a simultaneous PET-MR scanner. *EJNMMI Phys*. 2020;7:24.

22. Armanious K, Hepp T, Küstner T, et al. Independent attenuation correction of whole body [18F]FDG-PET using a deep learning approach with generative adversarial networks. *EJNMMI Res*. 2020;10:53.

23. Nuyts J, Man BD, Dupont P, Defrise M, Suetens P, Mortelmans L. Iterative reconstruction for helical CT: a simulation study. *Phys Med Biol*. 1998;43:729.

24. Oktay O, Schlemper J, Folgoc LL, et al. Attention U-net: learning where to look for the pancreas. 2018.

25. Cardoso MJ, Li W, Brown R, et al. MONAI: an open-source framework for deep learning in healthcare. 2022.

26. Watson C. Extension of Single Scatter Simulation to Scatter Correction of Time-of-Flight PET. *IEEE Trans Nucl Sci*. 2007;54:1679-1686.

27. Yan J, Schaefferkoetter J, Conti M, Townsend D. A method to assess image quality for low-dose PET: analysis of SNR, CNR, bias and image noise. *Cancer Imaging*. 2016;16:26.

Supplementary Files

This is a list of supplementary files associated with this preprint. Click to download.

- SupplementaryMaterial.pdf